A super-resolution technique to analyze single-crystal inelastic neutron scattering measurements using direct-geometry chopper spectrometers[a)]

Jiao Y. Y. Lin,[1, b)] Gabriele Sala,[1] and Matthew B. Stone[2]

[1)]*Spallation Neutron Source Second Target Station, Oak Ridge National Laboratory, Oak Ridge, Tennessee 37831, USA*

[2)]*Neutron Scattering Division, Oak Ridge National Laboratory, Oak Ridge, Tennessee 37831, USA*

(Dated: 9 January 2022)

Direct-geometry time-of-flight chopper neutron spectroscopy is instrumental in studying dynamics in liquid, powder, and single crystal systems. We report here that *real*-space techniques in optical imagery can be adapted to obtain *reciprocal*-space super resolution dispersion for phonon or magnetic excitations from single-crystal neutron spectroscopy measurements. The procedure to reconstruct super-resolution energy dispersion of excitations relies on accurate determination of the momentum and energy-dependent point spread function, and a dispersion correction technique inspired by an image disparity calculation technique commonly used in stereo imaging. Applying these methods to spinwave dispersion data from a virtual neutron experiment demonstrates $\sim$5-fold improvement over nominal energy resolution.

[b)]Electronic mail: linjiao@ornl.gov

I. INTRODUCTION

Inelastic neutron scattering (INS) is a powerful probe of fundamental excitations in solids, including those of vibrational or magnetic origins. Neutron scattering from these excitations are characterized by the 4-dimensional (4D) scattering function, $S(\mathbf{Q}, E)$, where $\mathbf{Q}$ is the momentum transfer and E the energy transfer. In recent years the use of highly pixelated detector arrays in conjunction with direct-geometry chopper spectrometer (DGS) instruments[1–7] has allowed for efficient measurements of single crystal 4D $S(\mathbf{Q}, E)$ functions over large ranges of $\mathbf{Q}$ and E. One single measurement of a single-crystal sample at a DGS instrument captures the sample scattering function $S(\mathbf{Q}, E)$ on a 3-dimensional(3D) manifold in the 4D $\mathbf{Q}, E$ space. Typically, a sample is rotated around a single axis, while maintaining a single wavelength (i.e. monochromatic energy) of incident neutrons, to scan the 4D $\mathbf{Q}, E$ volume. A series of 3D manifolds measured during the scan are then combined into the volumetric 4D dataset, allowing for extracting 2D slices at high-symmetry $\mathbf{Q}$ directions by using software packages such as Mantid[8], Horace[9], DAVE[10], Mslice[11], and Utsusemi[12]. This is done by integrating the measured scattering intensity along two of the four dimensions, yielding a scattering intensity as a function of the remaining two dimensions. Most often this is done to extract dispersion relations of fundamental excitations within crystalline solids by illustrating measured scattering intensity as a function of energy transfer along the vertical axis and a single direction in wave-vector transfer along the horizontal axis. These extracted dispersion data can be used to directly compare to model calculations of the materials dynamics in order to constrain or refine parameters in a model (i.e. the Hamiltonian). For magnetic systems, SpinW[13] is often used to fit spin-wave models to the experimentally obtained dispersion along multiple high-symmetry directions simultaneously. This allows one to obtain exchange parameters or other energy dependent terms in a model Hamiltonian which can represent the spin dynamics of the system.

Quantifying a crystalline material's vibrational or magnetic dispersion is key to understanding the system's dynamics. The accuracy of the measured dispersion (and that of the inferred quantities which define the dynamics such as exchange couplings or force constants) obtained from DGS experiments are bound by the instrument resolution. However, a significant number of measurements do not take into account instrumental resolution effects beyond the use of an analytical approximation of a single energy and wave-vector resolution of the instrument. DGS instrument resolution for the $S(\mathbf{Q}, E)$ scattering function is four-dimensional, and the effects of the resolu-

tion function is compounded by the slope and the curvature of the dispersion surface, making it cumbersome to accurately model. Given a set of instrument and experimental parameters such as chopper settings and the sample shape, the resolution function for DGS neutron scattering instruments still varies at different ($\mathbf{Q}$, E) points in the measured dynamical range. This resolution ellipsoid varies considerably across the detector array of the instrument as well as energy transfer. Furthermore, the resolution ellipsoid can have significant tilt that can lead to focusing and defocusing effects in the measured dispersion depending upon the slope of the dispersion relative to the tilt. This can make it difficult to accurately extract a model based upon the measured dispersions.

Recently it was demonstrated[14] that some super-resolution imagery techniques can be adapted to improve energy resolution in a phonon density of states measurement, $g(E)$, based upon neutron scattering techniques. This analysis was performed upon a measurement of the phonon density of states as a function of a single independent variable, energy transfer, which is a routine measurement for direct geometry chopper spectrometers measuring powder samples. In this work we introduce a super-resolution technique to improve the ability of extracting dispersion from inelastic neutron scattering measurements of single crystal samples. We use techniques inspired by image correlation methodologies to improve extraction of information from measurements as a function of two independent variables, energy and wave-vector transfer.

II. METHODS

A. Overview

Dispersion relations are obtained from single crystal measurements at DGS instruments by extracting slices of scattering intensity as a function of energy transfer, E, and wave-vector transfer, $\mathbf{Q}$, along high-symmetry directions in reciprocal space. These slices are obtained by integrating a portion of the measured reciprocal space along the two orthogonal reciprocal space directions to the direction of interest in the chosen slice. Constant $\mathbf{Q}$ cuts through these 2D slices can then be extracted by integrating a portion of the slices along wave-vector transfer and plotting the resulting scattering intensity as a function of energy transfer. For each constant $\mathbf{Q}$ cut through a single 2D slice, centers of peaks in the energy spectrum are recorded as the excitation energies for this particular $\mathbf{Q}$ value. The energy of these peak centers plotted as a function of $\mathbf{Q}$ are the measured dispersions. An analytic or numerical model of the dispersion can then be directly compared to

the experimentally determined dispersion values in order to determine model parameters. This is often done using non-linear curve fitting algorithms. This methodology of extracting dispersion parameters based upon peak location does not account for instrumental energy or wave-vector resolution. Such quantities may shift or skew peak locations and therefore would serve to skew any model parameters determined from comparison of peak positions to model dispersion. The method we present here calculates resolution based corrections to the measured dispersion functions.

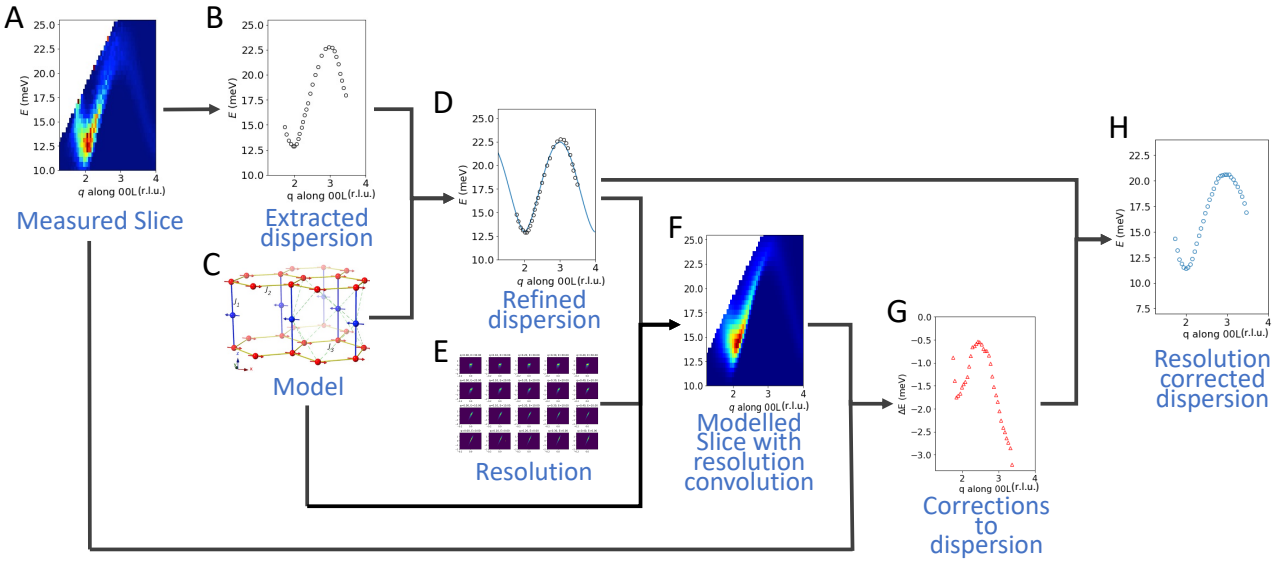

FIG. 1. Super-resolution dispersion workflow. An experimental dispersion (open circles in panel B and D) is first obtained from an experimental slice (panel A). This has been routinely done in single crystal DGS data analysis by finding the peak centers, E_j, of the constant q-cuts, $I(E;\, q_j)$, to form the dispersion data points $\{(q_j, E_j)\}$. The experimental dispersion is then fit to a dispersion model (an example is shown in panel C) to obtain modelled dispersion (the blue curve in panel D). This preliminary fitting provides a good starting point for the model parameters near the optimal values, and the subsequent steps will make super-resolution corrections. Resolution functions are calculated across the dynamical range of a slice (see panel E). The dispersion model (panel C) with the parameters obtained from fitting done in panel D is convolved with the resolution (panel E) to obtain a modelled slice (panel F). The disparity (panel G) between the modelled slice (F) and the experimental slice (A) is then calculated. Finally, the disparity (G) is used to correct the modelled dispersion (D) and obtain the corrected dispersion (panel H). The units of q are reciprocal lattice units (r.l.u.).

Figure 1 shows the steps of this dispersion correction workflow. An experimental slice is first obtained from data reduction (Figure 1A). A dispersion dataset is then obtained directly from the experimental slice, $E_{\mathrm{exp};0}(q)$, following the normal steps outlined earlier. This quantity is shown

as open symbols in Figure 1B. Those excitations are then fit to a dispersion model (in this case the spinwave model generated in SpinW) and relevant parameters (in this case exchange parameters) are obtained (Figure 1A, 1B, 1C, and 1D). The scattering cross section as a function of momentum transfer and energy transfer, including both the dispersion relation and the scattering amplitude, is now determined by the excitation model and relevant parameters. The next step is to obtain the instrument resolution function (Figure 1E). This can be achieved by using analytical calculations (This is often done for triple axis spectrometers[15–18]) or Monte Carlo neutron ray tracing simulations. More details can be found in section II B. By convolving the calculated scattering function with the instrument resolution function we can obtain the modelled slice (Figure 1F). Then we can compare the modelled slice and the experimental slice and obtain the energy shifts, $\Delta E(q)$ (Figure 1G), required to match the modeled slice to the experimental slice. This step is key to the super-resolution dispersion determination, and is further explained in section II C. The energy shifts obtained can then be applied to the model dispersion curve (from first fit to the experimental data) to obtain corrected dispersion curve (Figure 1H).

$$E_{\mathrm{exp;1}}(q) = E_{\mathrm{model;0}}(q) + \Delta E(q) \tag{1}$$

The focus of this work is to demonstrate that measured dispersion relations can be corrected taking into account resolution effects, but a natural further step is to fit the dispersion model to the corrected dispersion, $E_{\mathrm{exp;1}}(q)$, to obtain the corrected parameters for the Hamiltonian.

B. Resolution calculation and convolution

The 4D resolution function for a DGS instrument in measurements of single-crystal samples has been modelled analytically[19,20], using covariance matrix to simplify the treatment. It has also been calculated using Monte Carlo ray-tracing simulations[21–25], and was sometimes approximated using Gaussian functions when it was used in resolution convolution[26]. However, these corrections are not often taken into account in 4D DGS data analysis due to the complexity of the resolution convolution, and the computing resources required for fitting the dispersion model obtained from a highly pixelated detector array.

Incorporating resolution in the single crystal dispersion fitting workflow is difficult because:

- The resolution is 4D in nature, thus requiring a four-dimensional integration to convolve it with a model $S(\mathbf{Q}, E)$.

- The resolution function varies across the dynamical range, depending on the momentum and energy transfer. For example, as the energy transfer increases the energy resolution broadening decreases for direct geometry chopper spectrometers

- The resolution ellipsoid can have significant tilt that can lead to focusing and defocusing effects in the measured dispersion depending upon the slope of the dispersion relative to the tilt of the resolution ellipsoid.

- For some DGS instruments the energy resolution function is asymmetric as a result of the moderation process peculiar to neutron production in spallation neutron sources[27].

The last point here has very rarely been taken into account previously in single crystal dispersion fitting. Further, to fit the dispersion model incorporating the instrument resolution requires multiple evaluation of the dispersion model with varying parameters, as well as resolution convolution with the model for each set of parameters. The number of iterations depends on the optimization algorithm used and how close the initial guess was to the optimal model parameters. Such an optimization procedure can be demanding in both programming and computing resources.

The super-resolution procedure outlined in this work is agnostic to the technique of resolution calculation and convolution. In this work we have chosen to use a technique based on the Monte Carlo ray tracing simulation to illustrate the super-resolution methodology.

The MCViNE package[22,28] has been used to compute the resolution function for single crystal measurements at DGS instruments[22,24,25]. The procedure is reused here to simulate the resolution function (or point-spread function). The simulation starts with a beam simulation that matches experimental conditions such as incident energy and chopper settings. In order to calculate the energy and wave-vector resolution function with MCViNE, we use a virtual sample that has the same geometric shape and lattice parameters of the real sample to scatter neutrons in the vicinity of a particular set of momentum and energy transfer h,k,l,E. In the simulation we also take advantage of the measured UB matrix to orient the virtual sample just like what has been measured during the experiment. The virtual sample is also rotated around the vertical axis to a particular ω angle, similar to what happens in real measurements. The SEQUOIA detector system is simulated according to its specification such as the positions and orientations of all detector packs, the ^{3}He tube radius, length, and its spacing in the detector pack, the pressure of ^{3}He gas in the detector tubes, and the detector pixel height. Only events that arrive at the particular detector pixel and time-of-flight bin corresponding to the nominal h,k,l,E are collected. These detector events are

then reduced to $\tilde{h},\tilde{k},\tilde{l}$ and $\tilde{E}$. Those $\tilde{h},\tilde{k},\tilde{l},\tilde{E}$ values center around the nominal h,k,l,E, as expected. The differences between those $\tilde{h},\tilde{k},\tilde{l},\tilde{E}$ from the nominal h,k,l,E are kept in a list of dh,dk,dl,dE. The Monte Carlo ray tracing approach captures details of the 4D resolution function including, for example, the asymmetrical energy dependent line-shape mentioned previously.

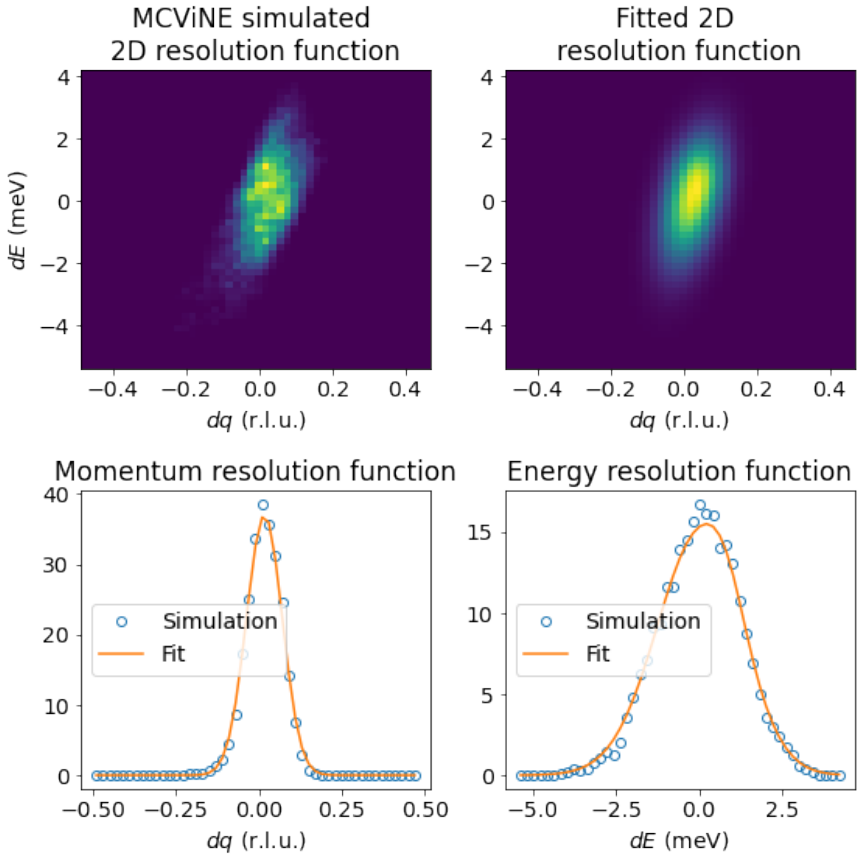

FIG. 2. Example resolution functions for the 00L slice at $q = L = 1.3,\ E = 5.0$. The 2D resolution function $R(q,E)$ is first simulated by using MCViNE, and then fitted to an analytical function.

To decrease the complexity of the resolution modeling and convolution, we perform them in two dimensions along the two axes of a slice. The details of the convolution will be presented later in this manuscript. We calculate a list of dq from the saved list of dh,dk,dl, where q is along the high-symmetry Q direction of the slice of interest. The dq,dE events are then histogrammed into a profile of the point spread function (PSF) for the 2D slice. This procedure is repeated for the points on a grid on the (q,E) plane. Each PSF at one grid point is fit to a sheared 2D function, with one axis which is ”energy-like" and has an asymmetric shape, and another axis which is ”momentum-like" and modelled as a gaussian. An example of this parameterization is presented

in Figure 2. Then an interpolation of the fitted parameters allows us to calculate the PSF function at any point in the q, E space.

Before convolution, the scattering intensities of the dispersion model are first integrated along the two **Q** directions perpendicular to the q direction for the slice of interest. Then the integrated data is convolved with the 2D resolution function modelled earlier to obtain the convoluted slice. This convolution method is a good approximation of the full 4D convolution, and an example is shown in section III B to demonstrate that.

C. Correction of dispersions

The basic idea here is to compare the two slices, namely the experimental slice (Figure 1A) and the resolution-convolved modelled slice (Figure 1F), to find the displacements between the dispersions in the two images which can then be used to correct the model. Finding displacements (or disparity) in two images has been a long-standing challenge in image processing. Stereo imaging techniques that uncover depth information of a scene captured in two images by finding disparity field between the images have been reviewed multiple times during the last few decades[29–31]. The techniques in traditional stereo vision find the disparity field $d(x,y)$ that minimizes the difference between the left image (image taken by a camera on the left) and the right image (image taken by a camera on the right) warped by the disparity:

$$\arg\min_{d(x,y)} \sum_{x,y} \left| I_l\left(x,\ y\right) - I_r\left(x,\ y - d(x,y)\right) \right|. \tag{2}$$

Used in this formula is the sum of the absolute differences, but often the sum of square differences, or normalized cross correlation are also used. $I_l(x,y)$ and $I_r(x,y)$ are left and right image intensities, and $d(x,y)$ is the displacement along y. Local methods for dense disparity calculation minimize cost functions (Equation 2) for local patches, while global methods[32,33] and semi-global methods[34] take the smoothness of disparity into account by constraining the disparity $d(x,y)$ using regularization. Advancements in computing techniques for disparity calculation have been proven useful in many fields of quantitative research, including remote-sensing and geophysics[35]. We aim to reuse the disparity calculation technique to estimate the displacement field between the experimental slice and the resolution-convolved model slice. In this first demonstrative work for application of image disparity calculation in the data analysis of neutron scattering measurements, we simplify the problem by limiting the slice to only one visible dispersion; therefore,

the displacement field can be simplified to be independent of E, and the minimization problem becomes

$$\arg\min_{\Delta E(q)} \sum_{q,E} |I_{exp}(q,E) - I_{model}(q,E-\Delta E(q))|. \quad (3)$$

The simplification of limiting the displacement field to be independent of E makes this optimization problem straightforward to program by using a SciPy[36] optimizer, for example.

III. RESULTS

A. The example dataset

In this work we illustrate the super-resolution dispersion technique using a synthetic dataset that resembles a real experimental dataset, for which the full analysis will be reported elsewhere[37]. In the experiment, a $Mn_3Si_2Te_6$ single-crystal sample was measured at the SEQUOIA instrument[3] with incident energy $E_i = 60$meV in the high flux mode, and the sample was rotated at least 180 degrees about the vertical axis, one degree per step, to cover a large volume in the reciprocal space. Slices along multiple high-symmetry directions show clear dispersions. The dispersions along those high-symmetry directions were obtained by finding centers of peaks in constant q cuts. They were fit to a Hamiltonian without on-site anisotropy, but which allows for anisotropic interactions for each of the exchange interactions to account for the spin-orbit coupling[37]

$$\begin{aligned} H =& J_1 \sum_{\langle i,j \rangle} [S_i^x S_j^x + S_i^y S_j^y + \Delta_1 S_i^z S_j^z] + \\ & J_2 \sum_{\langle i,j \rangle} [S_i^x S_j^x + S_i^y S_j^y + \Delta_2 S_i^z S_j^z] + \\ & J_3 \sum_{\langle i,j \rangle} [S_i^x S_j^x + S_i^y S_j^y + \Delta_3 S_i^z S_j^z]. \end{aligned} \quad (4)$$

Here, $\{J_i\}$ are exchange coefficients as shown in Figure 3 while $\{\Delta_i\}$ introduce anisotropy.

B. Synthetic data

First we build a synthetic dataset for which we know the exact model and parameters for the dispersion surface. The synthetic dataset is obtained from a virtual neutron experiment performed by using the MCViNE software. MCViNE contains a scattering kernel that scatters neutrons according to a dispersion surface that a user can define by using arbitrary analytical functions[22,23,28].

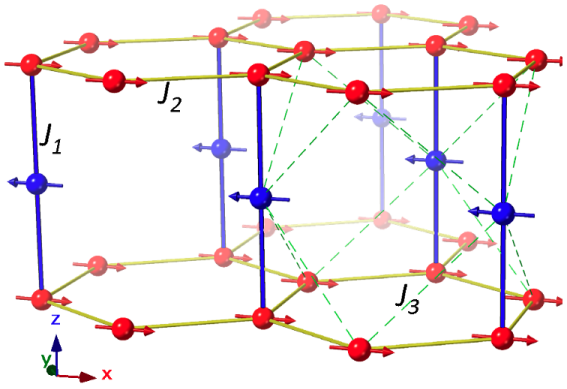

FIG. 3. The magnetic structure of $Mn_3Si_2Te_6$ and the exchange couplings between magnetic sites. The red and blue arrows follow the easy-plane directions of the spins in the ordered phase. The exchange J_1 is between the second nearest neighbor and shown as blue lines between Mn sites. The exchange J_2 is between the first nearest neighbor and shown as yellow lines within the honeycomb layers of the Mn sites. The exchange J_3 is between the third nearest neighbor, and shown as dashed green lines, which are only drawn for one portion of the lattice for clarity of the figure

Therefore, an analytical dispersion function similar to the dispersion surface of the spinwave model defined by Equation 4 was employed. The spin coupling constants used in the spinwave model in Equation 4 were $J_1 = 1.663$meV, $J_2 = 0.477$meV, $J_3 = 0.835$meV, $\Delta_1 = 0.390$, $\Delta_2 = -0.554$, $\Delta_3 = -0.431$. Analytical functions were used to approximate the dispersion and scattering intensity in the vicinity of the (002) wave-vector, and they were parameterized as

$$E(h,k,l) = E_b + E_a\left\{(1+0.61\sin^2\pi h)(1+0.61\sin^2\pi k)(1+\sin^{1.6}\frac{\pi l}{2}) - 1\right\} \quad (5)$$

$$S(h,k,l) = S0\frac{1}{1+\left(\frac{h}{\Gamma_h}\right)^2}\frac{1}{1+\left(\frac{k}{\Gamma_k}\right)^2}\frac{1}{1+\left(\frac{l-2}{\Gamma_l}\right)^2} \quad (6)$$

where $E_a = 11.6$ meV, $E_b = 9.05$ meV, $S0 = 14.8$, $\Gamma_h = \Gamma_l = 0.38$ r.l.u., $\Gamma_k = 0.35$ r.l.u.

Then we performed a virtual experiment of a sample with this analytical dispersion function and scattering intensity using MCViNE. The simulation and data reduction consists of the following steps:

- Beam simulation. We can reuse the beam simulation performed earlier for the resolution calculation as it contains all the information regarding the instrument.

- Sample scattering simulation. The sample has the same geometrical shape as the real sample, and with the dispersion defined in Equation 6. Simulations with a series of ω rotation

angles are performed, matching the real experiment.

- Detector simulation. The scattered neutrons are intercepted by the virtual SEQUOIA detector system, and the neutron events detected are saved in NeXus files, one for each ω angle.

- Reduction. The Mantid software[8] is then used to reduce the NeXus data files in the same way as the real experiment, and corresponding slices are made.

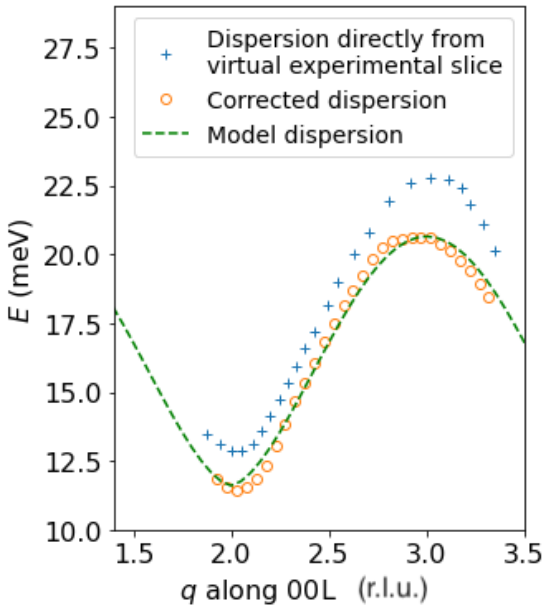

FIG. 4. Dispersion corrections for the virtual experimental data

Once we have the virtual experimental data, we perform the super-resolution workflow outlined in Figure 1 upon it. The results are shown in Figure 4. The corrected dispersion shows clear improvement in agreement with the model dispersion curve, compared to the original dispersion obtained directly from the experimental slice. The root-mean-square(RMS) difference between the experimental dispersion data and the model dispersion data was reduced from 1.59 meV to 0.32 meV, showing a nearly 5-fold improvement. It is worth noting that the nominal resolution of the SEQUOIA instrument at $E_i = 60$meV for the high-flux mode is $\sim$2meV. The fact that one single iteration of our super-resolution workflow can improve the dispersion data accuracy by 5-fold means our method is an efficient way to optimize dispersion model while taking into account the instrument resolution effect.

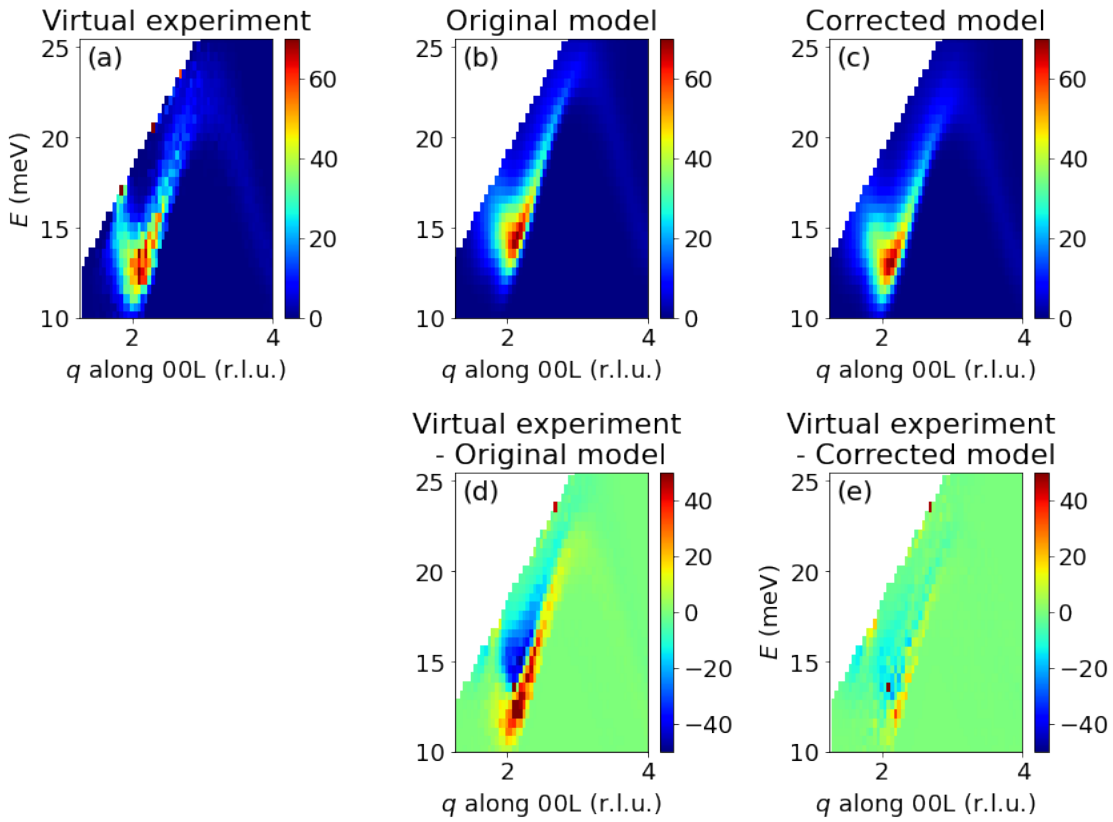

FIG. 5. 00L slices: (a) The 00L slice from the virtual experimental data obtained through the same data reduction procedure as the real experimental data using Mantid. (b) The analytical model using parameters fitted to the dispersion data obtained directly from the virtual experimental data, convolved by instrument resolution using the procedure explained in Section II B. (c) The analytical model using parameters fitted to the corrected dispersion data, convolved by instrument resolution. (d) The residual of subtracting the virtual experimental slice by the original dispersion model convolved with instrument resolution. The root mean square (RMS) of the residual is 10.8. (e) The residual of subtracting the virtual experimental slice by the corrected dispersion model convolved with instrument resolution. The RMS of the residual is reduced to 6.4.

Another way to check the improvement of the dispersion data is to observe the improvement of the fitting parameters in Equation 6. Table I presented the model parameters for the exact model, the fitted model without resolution correction, and the fitted model with resolution correction. Without the correction, we obtained $E_a = 12.93$meV and $E_b = 9.53$meV while fitting the dispersion data to Equation 6. Compared to the exact values of $E_a = 11.6$meV and $E_b = 9.05$meV, the fitted values are off by 1.33meV and 0.48meV, respectively. After correction, the fitting results are

TABLE I. Dispersion model parameters

Model	E_a (meV)	E_b (meV)
Exact	11.6	9.05
Without resolution correction: fit to dispersion data directly obtained from virtual experiment	12.93	9.53
With resolution correction: fit to corrected dispersion data	11.80	8.78

$E_a = 11.80$ and $E_b = 8.78$, and the errors are reduced to 0.20meV and 0.27meV.

An intuitive illustration of the improvement of the quality of the dispersion model is also presented in Figure 5. Here, Figure 5(a) is the 00L slice obtained from the virtual experiment data. Figure 5(b) is the resolution-convolved slice obtained from the dispersion model fitted to the original dispersion data from the virtual experiment without correction. It is clear that the dispersion is shifted upward in comparison to the virtual experimental data in panel (a). Figure 5(c) is the resolution-convolved slice obtained from the dispersion model fitted to the corrected dispersion data, and this slice agrees much better with the experimental slice in panel (a). This agreement is also a validation of our resolution convolution procedure. The better agreement of the corrected disperion model with the virtual experimental data is also evident in the residual plots shown in panel (d) and (e).

C. Real experimental data

We also applied the super-resolution dispersion workflow on the experimental SEQUOIA dataset described in section III A. In the previous section for the virtual experimental data, we apply the super-resolution procedure to one single slice. In comparison, for the real experimental data, we treat multiple slices along different **Q** directions. The first step of the workflow remains the same; the dispersion data for each slice is first obtained without considering the resolution effect. Then these dispersion data from multiple slices are fitted to the spin-wave model simultaneously to obtain the original set of the model parameters. The fitted model provides dispersion curves and scattering amplitudes for every slices, and they are convolved with resolution functions to obtained modelled slices. Each modelled slice is then compared to the corresponding experimental slice to obtain disparity curves, which are used to correct the dispersions. The cor-

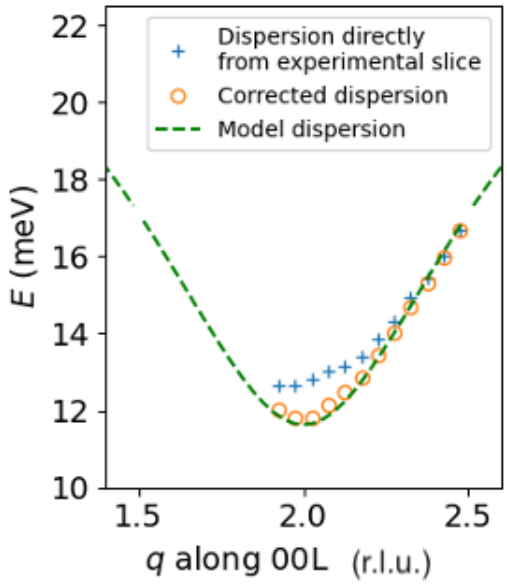

FIG. 6. Dispersion corrections for the real experimental slice along 00L near 002.

rected dispersions of all interested slices are then fit to the spin-wave model simultaneously again, yielding a new set of model parameters. One example of the dispersion correction is presented in Figure 6 for the 00L dispersion. Energy corrections in the order of 1meV are found near 002. The full dispersion correction data are reported elsewhere [37].

IV. CONCLUSION

A new technique to obtain super-resolution dispersions along high-symmetry **Q** directions for single crystal measurements employing direct geometry neutron spectrometers is developed. This is done by computing the disparity curve between the resolution-convolved-model slice and the experimental slice and then applying the disparity to correct the dispersion. Here the resolution-convolved slice was obtained by convolving the resolution with the scattering intensity of a dispersion model that was fit to the experimental dispersions obtained without any consideration of instrument resolution. The disparity of the slices was obtained by minimizing the difference between the experimental slice and the modelled slice warped by disparity, subjecting to the total variation regularization. The technique clearly shows improvements in the determination of dispersions and it is computationally faster, since classical methods would have required multiple iterations of model evaluation and resolution convolution with many more sets of model parame-

ters. We show that this method can achieve 5-fold super-resolution w.r.t nominal resolution of the SEQUOIA[38] instrument. The demonstration is facilitated by a MCViNE-based virtual experiment, which provides the virtual experimental data and the known target model to check the effectiveness of the super-resolution technique.

This super-resolution dispersion technique is limited by the signal-to-noise ratio as other imaging techniques. The 2D resolution convolution method used in this work can be updated to use 4D resolution convolution to improve the accuracy and the universality of this approach. More sophisticated disparity computation techniques can be adapted to remove the limit of single dispersion per slice. Finally, many image processing techniques may find various applications in neutron data analysis. Another potential application of the disparity calculation technique is to detect super-resolution variations in dispersions w.r.t temperature/pressure under which the sample is measured.

This work focuses on the correction of the dispersion relation $E(q)$ between the excitation energy E and its momentum q. It can be envisioned that the super-resolution techniques developed in the previous work for powder DGS data[14] can be extended and combined with techniques developed in this work to reconstruct super-resolution $I(q, E)$ slices, reducing the influence of the instrument broadening, and providing information on the intrinsic line-widths of the excitations, $\Gamma_E(q)$.

ACKNOWLEDGMENTS

The authors thank Hillary Smith, Brent Fultz, Garrett Granroth, and Doug Abernathy for fruitful discussions. This work was partially supported by the Department of Energy, Laboratory Directed Research and Development SEED funding, under contract DE-AC05-00OR22725. Work at Spallation Neutron Source at Oak Ridge National Laboratory (ORNL) was supported by the Scientific User Facilities Division, Office of Basic Energy Sciences, US Department of Energy (DOE). This research also used resources of the Spallation Neutron Source Second Target Station Project at ORNL. ORNL is managed by UT-Battelle LLC for DOE's Office of Science, the single largest supporter of basic research in the physical sciences in the United States.

DATA AVAILABILITY

The data that support the findings of this study are available from the corresponding author upon reasonable request.

REFERENCES

[1]R. Bewley, R. Eccleston, K. McEwen, S. Hayden, M. Dove, S. Bennington, J. Treadgold, and R. Coleman, "Merlin, a new high count rate spectrometer at isis," Physica B: Condensed Matter **385-386**, 1029 – 1031 (2006).

[2]D. L. Abernathy, M. B. Stone, M. Loguillo, M. Lucas, O. Delaire, X. Tang, J. Lin, and B. Fultz, "Design and operation of the wide angular-range chopper spectrometer arcs at the spallation neutron source," Review of Scientific Instruments **83**, 015114 (2012).

[3]G. E. Granroth, A. I. Kolesnikov, T. E. Sherline, J. P. Clancy, K. A. Ross, J. P. C. Ruff, B. D. Gaulin, and S. E. Nagler, "Sequoia: A newly operating chopper spectrometer at the sns," Journal of Physics: Conference Series **251**, 012058 (2010).

[4]G. Ehlers, A. A. Podlesnyak, J. L. Niedziela, E. B. Iverson, and P. E. Sokol, "The new cold neutron chopper spectrometer at the spallation neutron source: Design and performance," Review of Scientific Instruments **82**, 085108 (2011), https://doi.org/10.1063/1.3626935.

[5]R. Bewley, J. Taylor, and S. Bennington., "Let, a cold neutron multi-disk chopper spectrometer at isis," Nuclear Instruments and Methods in Physics Research Section A: Accelerators, Spectrometers, Detectors and Associated Equipment **637**, 128 – 134 (2011).

[6]R. Kajimoto, M. Nakamura, Y. Inamura, F. Mizuno, K. Nakajima, S. Ohira-Kawamura, T. Yokoo, T. Nakatani, R. Maruyama, K. Soyama, K. Shibata, K. Suzuya, S. Sato, K. Aizawa, M. Arai, S. Wakimoto, M. Ishikado, S.-i. Shamoto, M. Fujita, H. Hiraka, K. Ohoyama, K. Yamada, and C.-H. Lee, "The fermi chopper spectrometer 4seasons at j-parc," Journal of the Physical Society of Japan **80**, SB025 (2011), https://doi.org/10.1143/JPSJS.80SB.SB025.

[7]S. Itoh, T. Yokoo, S. Satoh, S. ichiro Yano, D. Kawana, J. Suzuki, and T. J. Sato, "High resolution chopper spectrometer (hrc) at j-parc," Nuclear Instruments and Methods in Physics Research Section A: Accelerators, Spectrometers, Detectors and Associated Equipment **631**, 90 – 97 (2011).

[8]O. Arnold, J.-C. Bilheux, J. Borreguero, A. Buts, S. I. Campbell, L. Chapon, M. Doucet, N. Draper, R. F. Leal, M. Gigg, *et al.*, "Mantid—data analysis and visualization package for neutron scattering and μ sr experiments," Nuclear Instruments and Methods in Physics Research Section A: Accelerators, Spectrometers, Detectors and Associated Equipment **764**, 156–166 (2014).

[9]R. Ewings, A. Buts, M. Le, J. Van Duijn, I. Bustinduy, and T. Perring, "Horace: software for the analysis of data from single crystal spectroscopy experiments at time-of-flight neutron instruments," Nuclear Instruments and Methods in Physics Research Section A: Accelerators, Spectrometers, Detectors and Associated Equipment **834**, 132–142 (2016).

[10]R. T. Azuah, L. R. Kneller, Y. Qiu, P. L. Tregenna-Piggott, C. M. Brown, J. R. Copley, and R. M. Dimeo, "Dave: a comprehensive software suite for the reduction, visualization, and analysis of low energy neutron spectroscopic data," Journal of Research of the National Institute of Standards and Technology **114**, 341 (2009).

[11]"Mslice," `http://mslice.isis.rl.ac.uk`, accessed: 2021-07-31.

[12]Y. Inamura, T. Nakatani, J. Suzuki, and T. Otomo, "Development status of software "utsusemi" for chopper spectrometers at mlf, j-parc," Journal of the Physical Society of Japan **82**, SA031 (2013).

[13]S. Toth and B. Lake, "Linear spin wave theory for single-q incommensurate magnetic structures," Journal of Physics: Condensed Matter **27**, 166002 (2015).

[14]F. Islam, J. Y. Lin, R. Archibald, D. L. Abernathy, I. Al-Qasir, A. A. Campbell, M. B. Stone, and G. E. Granroth, "Super-resolution energy spectra from neutron direct-geometry spectrometers," Review of Scientific Instruments **90**, 105109 (2019).

[15]A. Zheludev, "Reslib 3.4," (2007).

[16]M. Popovici, "On the resolution of slow-neutron spectrometers. iv. the triple-axis spectrometer resolution function, spatial effects included," Acta Crystallographica Section A: Crystal Physics, Diffraction, Theoretical and General Crystallography **31**, 507–513 (1975).

[17]N. t. Chesser and J. Axe, "Derivation and experimental verification of the normalized resolution function for inelastic neutron scattering," Acta Crystallographica Section A: Crystal Physics, Diffraction, Theoretical and General Crystallography **29**, 160–169 (1973).

[18]M. t. Cooper and R. Nathans, "The resolution function in neutron diffractometry. i. the resolution function of a neutron diffractometer and its application to phonon measurements," Acta Crystallographica **23**, 357–367 (1967).

[19]T. Perring, "The resolution function of the chopper spectrometer het at isis," in *Journal of Neutron Research, Proceedings of the Twelfth Meeting of the International Collaboration on Advanced Neutron Sources (ICANS-XII)(Cosener's House, Abingdon, UK, 1993) pp. I-328* (1993).

[20]N. Violini, J. Voigt, S. Pasini, and T. Brückel, "A method to compute the covariance matrix of wavevector-energy transfer for neutron time-of-flight spectrometers," Nuclear Instruments and Methods in Physics Research Section A: Accelerators, Spectrometers, Detectors and Associated Equipment **736**, 31–39 (2014).

[21]G. E. Granroth and S. E. Hahn, "Monte carlo simulation of the resolution volume for the sequoia spectrometer," in *EPJ Web of Conferences*, Vol. 83 (EDP Sciences, 2015) p. 03006.

[22]J. Y. Lin, F. Islam, G. Sala, I. Lumsden, H. Smith, M. Doucet, M. B. Stone, D. L. Abernathy, G. Ehlers, J. F. Ankner, *et al.*, "Recent developments of mcvine and its applications at sns," Journal of Physics Communications **3**, 085005 (2019).

[23]J. Leiner, H. O. Jeschke, R. Valentí, S. Zhang, A. Savici, J. Lin, M. Stone, M. Lumsden, J. Hong, O. Delaire, *et al.*, "Frustrated magnetism in mott insulating (v 1- x cr x) 2 o 3," Physical Review X **9**, 011035 (2019).

[24]T. Lanigan-Atkins, S. Yang, J. L. Niedziela, D. Bansal, A. F. May, A. A. Puretzky, J. Lin, D. M. Pajerowski, T. Hong, S. Chi, *et al.*, "Extended anharmonic collapse of phonon dispersions in sns and snse," Nature communications **11**, 1–9 (2020).

[25]Y. Chen, J. Gaudet, S. Dasgupta, G. Marcus, J. Lin, T. Chen, T. Tomita, M. Ikhlas, Y. Zhao, W. Chen, *et al.*, "Antichiral spin order, its soft modes, and their hybridization with phonons in the topological semimetal mn 3 ge," Physical Review B **102**, 054403 (2020).

[26]S. E. Hahn, A. A. Podlesnyak, G. Ehlers, G. E. Granroth, R. S. Fishman, A. I. Kolesnikov, E. Pomjakushina, and K. Conder, "Inelastic neutron scattering studies of yfeo3," Physical Review B **89**, 014420 (2014).

[27]S. Ikeda and J. M. Carpenter, "Wide-energy-range, high-resolution measurements of neutron pulse shapes of polyethylene moderators," Nuclear Instruments and Methods in Physics Research Section A: Accelerators, Spectrometers, Detectors and Associated Equipment **239**, 536–544 (1985).

[28]J. Y. Y. Lin, H. L. Smith, G. E. Granroth, D. L. Abernathy, M. D. Lumsden, B. Winn, A. A. Aczel, M. Aivazis, and B. Fultz, "Mcvine – an object oriented monte carlo neutron ray tracing simulation package." Nuclear Instruments and Methods in Physics Research Section A: Accelerators, Spectrometers, Detectors and Associated Equipment **810**, 86–99 (2016).

[29]S. T. Barnard and M. A. Fischler, "Computational stereo," ACM Computing Surveys (CSUR) **14**, 553–572 (1982).

[30]D. Scharstein and R. Szeliski, "A taxonomy and evaluation of dense two-frame stereo correspondence algorithms," International journal of computer vision **47**, 7–42 (2002).

[31]N. Lazaros, G. C. Sirakoulis, and A. Gasteratos, "Review of stereo vision algorithms: from software to hardware," International Journal of Optomechatronics **2**, 435–462 (2008).

[32]V. Kolmogorov and R. Zabih, "Computing visual correspondence with occlusions using graph cuts," in *Proceedings Eighth IEEE International Conference on Computer Vision. ICCV 2001*, Vol. 2 (IEEE, 2001) pp. 508–515.

[33]A. Klaus, M. Sormann, and K. Karner, "Segment-based stereo matching using belief propagation and a self-adapting dissimilarity measure," in *18th International Conference on Pattern Recognition (ICPR'06)*, Vol. 3 (IEEE, 2006) pp. 15–18.

[34]H. Hirschmuller, "Accurate and efficient stereo processing by semi-global matching and mutual information," in *2005 IEEE Computer Society Conference on Computer Vision and Pattern Recognition (CVPR'05)*, Vol. 2 (IEEE, 2005) pp. 807–814.

[35]F. Herman, O. Beyssac, M. Brughelli, S. N. Lane, S. Leprince, T. Adatte, J. Y. Lin, J.-P. Avouac, and S. C. Cox, "Erosion by an alpine glacier," Science **350**, 193–195 (2015).

[36]P. Virtanen, R. Gommers, T. E. Oliphant, M. Haberland, T. Reddy, D. Cournapeau, E. Burovski, P. Peterson, W. Weckesser, J. Bright, S. J. van der Walt, M. Brett, J. Wilson, K. J. Millman, N. Mayorov, A. R. J. Nelson, E. Jones, R. Kern, E. Larson, C. J. Carey, İ. Polat, Y. Feng, E. W. Moore, J. VanderPlas, D. Laxalde, J. Perktold, R. Cimrman, I. Henriksen, E. A. Quintero, C. R. Harris, A. M. Archibald, A. H. Ribeiro, F. Pedregosa, P. van Mulbregt, and SciPy 1.0 Contributors, "SciPy 1.0: Fundamental Algorithms for Scientific Computing in Python," Nature Methods **17**, 261–272 (2020).

[37]"Ferrimagnetic spin-waves in the honeycomb and triangular layers of $Mn_3Si_2Te_6$," To be published elsewhere.

[38]G. Granroth, A. Kolesnikov, T. Sherline, J. Clancy, K. Ross, J. Ruff, B. Gaulin, and S. Nagler, "Sequoia: A newly operating chopper spectrometer at the sns," in *Journal of Physics: Conference Series*, Vol. 251 (IOP Publishing, 2010) p. 012058.